Semi-Spectral Method for the Wigner equation

O. Furtmaier,[1,*] S. Succi,[2,†] and M. Mendoza[1,‡]

[1] *ETH Zürich, Institute for Building Materials, Schafmattstrasse 6 CH-8093 Zürich*
[2] *Istituto per le Applicazioni del Calcolo C.N.R, Via dei Taurini 19, 00185 Rome, Italy*

We propose a numerical method to solve the Wigner equation in quantum systems of spinless, non-relativistic particles. The method uses a spectral decomposition into $L^2(\mathbb{R}^d)$ basis functions in momentum-space to obtain a system of first-order advection-reaction equations. The resulting equations are solved by splitting the reaction and advection steps so as to allow the combination of numerical techniques from quantum mechanics and computational fluid dynamics by identifying the skew-hermitian reaction matrix as a generator of unitary rotations. The method is validated for the case of particles subject to a one-dimensional (an-)harmonic potential using finite-differences for the advection part. Thereby, we verify the second order of convergence and observe non-classical behavior in the evolution of the Wigner function.

Keywords: Wigner equation, Spectral method, Reaction-advection

I. INTRODUCTION

The Wigner formalism, also known as quantum mechanics in phase space [1], provides an alternative but equivalent description of quantum mechanics in trems of a (quasi)-distribution function of the particle position and momentum. It has proven to provide a helpful supplement to operator methods in Hilbert space as well as to path integral formulations, and has offered new insights into the relation between quantum and classical physics, as it does not discriminate between coordinate and momentum space. For instance, it has been a fruitful perspective for the study of quantum chaos. In addition, it offers the opportunity to systematically consider quantum corrections to the classical dynamics by expanding the *quantum Liouville equation* around $\hbar \approx 0$. Nowadays, it is also a valuable tool in the fields of quantum optics as well as nuclear, plasma and semiconductor physics to describe transport processes, for example, in open quantum systems [1]. The Wigner function, introduced by E. Wigner in Ref. [2], is the Weyl transformation of the density matrix and a quasi-probability distribution that can "intuitively" account for scattering and decoherence effects in quantum systems [3, 4]. It differs from a classical probability distributions as it can change sign during the evolution especially in regions where quantum interference effects become important.

Since the Wigner equation was introduced in 1932, it has been tackled by various numerical approaches, such as finite differences [5, 6], Fourier spectral collocation [7, 8], deterministic particle [9, 10], and Monte-Carlo [11, 12]. Here, we extend the technique described in Refs. [7, 8] to arbitrary basis functions $\phi_n(\vec{p})$ of $L^2(\mathbb{R}^d)$ in momentum-space and reveal the underlying mathematical structure of the resulting infinite-dimensional set of reaction-advection equations. By using this formulation we show that the action of the potential on the Wigner function is a unitary rotation of its coefficient vector, whereas the advection operation can be discretized by various techniques used in computational fluid dynamics, such as finite difference, finite volume or finite element, cf. Ref. [13]. In that way, one is able to construct a finite element simulation of the Wigner evolution. Employing a more general basis we assume that the higher computational costs of our method, $\mathcal{O}(N^2)$, compared to $\mathcal{O}(N \log N)$ for the spectral Fourier decomposition are outweighed by a smaller number N of basis functions to obtain the same order of accuracy through focusing the computational effort to regions of interest, as for example in the case of Wigner functions that are strongly localized in momentum-space, such as particles in a periodic potential, cf. Bloch's theorem and Ref. [14]. In addition, the "artificial" periodization of the Wigner function can be avoided, which may mitigate the self-interaction of the distribution at the domain boundaries of the simulation that is present for the Fourier basis choice, cf. Ref. [15].

This article is organized as follows. First, we give an introduction to the Wigner formalism and present the properties of the Wigner equation, especially for the pseudo-differential operator. In section III we show the details of the numerical method to handle the obtained multi-dimensional reaction-advection equation. Thirdly, we validate the technique by simulating a one-dimensional (an-)harmonic oscillator, which offers the opportunity to compare with an analytical solution, cf. Ref. [16], such that we can perform a convergence analysis, and to observe quantum effects when the anharmonic potential is used. To study tunneling phenomena, we show the evolution of bounded states in the double well potential and measure the spread as well as the covariance of the Wigner function in phase space. In the last section, we will highlight the strengths and weaknesses of the approach.

* oliverfu@ethz.ch
† succi@iac.cnr.it
‡ mmendoza@ethz.ch

II. WIGNER FORMALISM

Our aim is to simulate the time-evolution of the Wigner function $w(\tau,\vec{q},\vec{p})$ of a d-dimensional system of non-relativistic spinless particles of mass m subject to the potential $U(\tau,\vec{q})$, based on the Wigner equation

$$0=\partial_\tau w+\frac{\vec{p}}{m}\cdot\vec{\nabla}_q w+\Theta[U]w\ , \tag{1}$$

$$\Theta[U]\equiv\frac{\imath}{\hbar}\left[U(\tau,\vec{q}+\imath\hbar\vec{\nabla}_p/2)-U(\tau,\vec{q}-\imath\hbar\vec{\nabla}_p/2)\right]\ . \tag{2}$$

The independent variables are time τ, space $\vec{q}$ and momentum $\vec{p}$ respectively. Hence, the Wigner function itself has the dimension h^{-d}, since it fulfills

$$\int\limits_{\mathbb{R}^d}\mathrm{d}\vec{q}\int\limits_{\mathbb{R}^d}\mathrm{d}\vec{p}\ w(\tau,\vec{q},\vec{p})=N_p\ , \tag{3}$$

where N_p is the number of particles in the system. To have an easier grasp on the equation, we make it dimensionless. First of all, we measure the Wigner function with respect to $\hbar^d$, i.e. we introduce the dimensionless Wigner function $W(\tau,\vec{q},\vec{p})\equiv\hbar^d w(\tau,\vec{q},\vec{p})/N_p$, and we employ the following scaling relations

$$\vec{x}=\vec{q}/l\ ,\ t=\tau/T\ ,\ \vec{v}=\frac{T}{lm}\vec{p}\ ,\ V(t,\vec{x})=U(\tau,\vec{q})/\bar{U}\ ,$$

described in Ref. [17]. Thus, we obtain the dimensionless Wigner equation

$$0=\partial_t W+\vec{v}\cdot\vec{\nabla}_x W+\Theta[V]W\ , \tag{4}$$

$$\Theta[V]=\frac{\imath B}{\epsilon}\left[V\left(t,\vec{x}+\frac{\imath\epsilon}{2}\vec{\nabla}_v\right)-V\left(t,\vec{x}-\frac{\imath\epsilon}{2}\vec{\nabla}_v\right)\right]\ , \tag{5}$$

where we have introduced the dimensionless constants

$$\epsilon\equiv\frac{\hbar T}{l^2m}\ ,\ B\equiv\frac{\bar{U}T^2}{l^2m}\ , \tag{6}$$

which we call *effective* Planck's constant and potential strength, respectively. The names are not arbitrary and reflect the natural occurrence of these numbers in the dimensionless formulation of the dynamics. For instance, Eq. (3) directly translates into

$$\epsilon^{-d}\int\limits_{\mathbb{R}^d}\mathrm{d}\vec{x}\int\limits_{\mathbb{R}^d}\mathrm{d}\vec{v}\ W(t,\vec{x},\vec{v})=1\ , \tag{7}$$

where we have replaced Planck's constant by its scaled counterpart; the Wigner transform of a pure state Ψ becomes

$$W=\int\limits_{\mathbb{R}^d}\mathrm{d}\vec{y}\ \Psi^*\left(t,\vec{x}+\frac{\vec{y}}{2}\right)\Psi\left(t,\vec{x}-\frac{\vec{y}}{2}\right)\frac{e^{\imath\vec{v}\cdot\vec{y}/\epsilon}}{(2\pi)^d}\ , \tag{8}$$

where $\Psi(t,\vec{x})\equiv l^{d/2}\psi(\tau,\vec{q})$ is the dimensionless wave function in position space; the dimensionless time-dependent Schrödinger equation reads

$$\imath\epsilon\partial_t\Psi=\left[|\hat{\vec{v}}|^2/2+B\hat{V}(t,\vec{x})\right]\Psi\ , \tag{9}$$

and the canonical commutation relation is written as

$$[\hat{x}_j,\hat{v}_k]=\imath\epsilon\delta_{j,k}\ . \tag{10}$$

The symbol $\Theta[V]$ stands for the pseudo-differential operator, whose action on W can be written as an integral

$$\Theta[V]W=\frac{\imath B}{\epsilon}\int\limits_{\mathbb{R}^d}\mathrm{d}\vec{\eta}\ \delta V(t,\vec{x},\vec{\eta})\hat{W}(t,\vec{x},\vec{\eta})e^{-\imath\vec{\eta}\cdot\vec{v}}\ , \tag{11}$$

$$\delta V(t,\vec{x},\vec{\eta})\equiv V\left(t,\vec{x}+\frac{\epsilon}{2}\vec{\eta}\right)-V\left(t,\vec{x}-\frac{\epsilon}{2}\vec{\eta}\right), \tag{12}$$

$$\hat{W}(t,\vec{x},\vec{\eta})=\frac{1}{(2\pi)^d}\int\limits_{\mathbb{R}^d}\mathrm{d}\vec{p}\ W(t,\vec{x},\vec{p})e^{\imath\vec{\eta}\cdot\vec{p}}\ . \tag{13}$$

If the potential is locally well-approximated by a Taylor series around $\epsilon\approx 0$ we can write

$$V(t,\vec{x}+\epsilon\vec{\eta}/2)\approx\sum_{|\lambda|=0}^{\infty}(\epsilon/2)^{|\lambda|}\frac{D_x^\lambda V(t,\vec{x})}{\lambda!}\vec{\eta}^\lambda\ , \tag{14}$$

where λ is a multi-index of dimension d, i.e. $|\lambda|\equiv\sum_{i=1}^d\lambda_i$, $\lambda!=\prod_{i=1}^d\lambda_i!$, and $\vec{\eta}^\lambda\equiv\prod_{j=1}^d\eta_j^{\lambda_j}$. Therefore, the action of the pseudo-differential operator on the Wigner function reads

$$\Theta[V]W=-B\sum_{|\lambda|\in\mathbb{N}_{odd}}(\imath\epsilon/2)^{|\lambda|-1}\frac{1}{\lambda!}\left(D_x^\lambda V\right)\left(D_v^\lambda W\right)\ . \tag{15}$$

$\mathbb{N}_{odd}$ stands for strictly positive odd integers, such that the sum is always real. For this treatment, the potential needs to be an *analytic function* defined on an open set $D\subset\mathbb{R}^d\times\mathbb{R}$, i.e. explicit dependence on time is possible. This implies two important properties for us. Firstly, the function is locally given by a convergent power or Taylor series. Secondly, one can find an upper bound for all derivatives of the function, since for every compact set $K\subset D$, for all $(t,\vec{x})\in K$, and for all $|\lambda|\in\mathbb{N}_0$ there exists a constant C such that

$$|D_x^\lambda V|\leq C^{|\lambda|+1}\lambda!\ . \tag{16}$$

Hence, by choosing the right time and length scale (T,l) for the problem one can find a convergent power series representation of the pseudo-differential operator. The correct choice means

$$\lim_{|\lambda|\to\infty}\left(\frac{C\epsilon}{2}\right)^{|\lambda|}=0\ , \tag{17}$$

such that the series in Eq. (15) converges (locally) uniformly under the assumption that $D_v^\lambda W$ is bounded.

A. General properties

Expanding the Wigner function in momentum-space into a set of orthonormal basis functions $\{\phi_k\}_{k\in\mathbb{N}}$ of

$L^2(\mathbb{R}^d)$ with the inner product

$$\langle \phi_i, \phi_j \rangle_2 \equiv \int_{\mathbb{R}^d} \mathrm{d}\vec{v}\ \phi_i^*(\vec{v})\phi_j(\vec{v}) = \delta_{i,j}\ , \tag{18}$$

meaning that

$$W(t,\vec{x},\vec{v}) = \sum_{k\in\mathbb{N}} a_k(t,\vec{x})\ \phi_k(\vec{v})\ , \tag{19}$$

we can rewrite the Wigner equation, Eq. (4), into an infinite system of linear, first-order partial differential equations (PDEs) for the coefficients $a_k(t,\vec{x}) \in \mathbb{C}$. The system can be derived by using the orthonormality property of the basis functions, Eq. (18). Depending on the choice of the basis we will find different sets of PDEs. In general, all the sets can be written as a multi-dimensional *reaction-advection* equation

$$\partial_t \vec{a} + \sum_{i=1}^{d} A^{(i)} \partial_{x_i} \vec{a} + M_V(t,\vec{x})\vec{a} = \vec{0}\ , \tag{20}$$

where $A^{(i)}, M_V(t,\vec{x})$ are square matrices and $\vec{a} = (a_1, a_2, a_3, \dots)$ is the coefficient vector. Independent of the basis choice, the matrix $M_V(t,\vec{x})$ is *skew-hermitian*, which can be demonstrated employing Eq. (15) or Eq. (11). When using formula (15) we have to assume that the basis functions are $C^\infty(\mathbb{R}^d)$. Under this condition we can shift the uneven derivatives, $|\lambda| \in \mathbb{N}_{odd}$, which appear as summands in the pseudo-differential operator, to show the skew-hermiticity. Demonstrating this property for a *general* set of basis functions of $L^2(\mathbb{R}^d)$, i.e. even non-differentiable, we use Eq. (11) to write

$$\begin{aligned}(M_V\vec{a})_k =& \int_{\mathbb{R}^d} \mathrm{d}\vec{v}\ \phi_k^*(\vec{v})\left(\Theta[V]W\right)(t,\vec{x},\vec{v}) && (21)\\ =& \frac{\imath B}{\epsilon}\int_{\mathbb{R}^d} \mathrm{d}\vec{\eta}\ \delta V(t,\vec{x},\vec{\eta})\hat{W}(t,\vec{x},\vec{\eta}) \\ & \times \int_{\mathbb{R}^d} \mathrm{d}\vec{v}\ \phi_k^*(\vec{v}) e^{-\imath\vec{v}\cdot\vec{\eta}}\ , && (22)\end{aligned}$$

from which we conclude

$$\begin{aligned}(M_V)_{k,l} =& \frac{\imath B}{(2\pi)^d\epsilon}\int_{\mathbb{R}^d} \mathrm{d}\vec{\eta}\ \delta V(t,\vec{x},\vec{\eta}) \\ & \times \int_{\mathbb{R}^d\times\mathbb{R}^d} \mathrm{d}\vec{v}\mathrm{d}\vec{p}\ \phi_k^*(\vec{v}) e^{-\imath\vec{v}\cdot\vec{\eta}}\phi_l(\vec{p}) e^{\imath\vec{p}\cdot\vec{\eta}}\ . \end{aligned} \tag{23}$$

This equation confirms the skew-hermiticity of the matrix representation of the pseudo-differential operator, which is an important property for the stability of the proposed algorithm as we will see in the next section. An example of this matrix representation is shown in appendix A. The entries of the matrix $A^{(i)}$ are given by

$$\left(A^{(i)}\right)_{k,l} = \int_{\mathbb{R}^d} \mathrm{d}\vec{v}\ \phi_k^*(\vec{v}) v_i \phi_l(\vec{v})\ , \tag{24}$$

which shows that it is *hermitian*.

III. NUMERICAL METHOD

For the numerical treatment, the expansion in Eq. (19), is cut at the index N, i.e. we assume all higher coefficients to be zero. The problem is hence shifted to the time-evolution of the N-dimensional coefficient vector with the initial condition

$$\vec{a}(t_0,\vec{x}) = \int_{\mathbb{R}^d} \mathrm{d}\vec{v}\ W(t_0,\vec{x},\vec{v})\vec{\phi}(\vec{v})\ , \tag{25}$$

where $\vec{\phi} = (\phi_1, \phi_2, \dots, \phi_N)$. Therefore, we work with a finite set of N balance equations (PDEs) in the form of Eq. (20). It is important to note that, thanks to the Cauchy-Kowaleski theorem, see Ref. [18], we know that the system will *locally* have a *unique analytical* solution if the coefficient matrix M_V is an analytic function. This condition is sufficient, since the matrices $A^{(i)}$ are constant. In addition, we would like to mention that this does not necessarily apply if M_V belongs to the larger group of smooth functions, see Levy's argument in Ref. [18].

A. Operator-splitting

To proceed with the problem we use an operator-splitting technique ("divide-and-conquer"), i.e. we separate the action of the "streaming",

$$\mathcal{S}\vec{a} \equiv -\sum_{i=1}^{d} A^{(i)}\partial_{x_i}\vec{a}\ , \tag{26}$$

and "forcing",

$$\mathcal{F}_t\vec{a} \equiv -M_V(t,\vec{x})\vec{a}\ , \tag{27}$$

operators to apply them sequentially. First, we discretize the time interval from zero to t in N_t periods of duration δt. Then we can write the approximated solution to Eq. (20) as

$$\begin{aligned}\vec{a}(t,\vec{x}) &\approx \overleftarrow{\prod_{k=0}^{N_t-1}} \exp\left(\mathcal{S}\delta t + \int_{k\delta t}^{(k+1)\delta t} \mathrm{d}t'\ \mathcal{F}_{t'}\right)\vec{a}_0(\vec{x}), \\ &\approx \overleftarrow{\prod_{k=0}^{N_t-1}} e^{\mathcal{S}\delta t}\exp\left(\int_{k\delta t}^{(k+1)\delta t} \mathrm{d}t'\ \mathcal{F}_{t'}\right)\vec{a}_0(\vec{x})\ , \\ &\approx \overleftarrow{\prod_{k=0}^{N_t-1}} e^{\mathcal{S}\delta t}e^{\mathcal{F}_{k\delta t}\delta t}\vec{a}_0(\vec{x}) + \mathcal{O}(\delta t)\ , \end{aligned} \tag{28}$$

where in the first step we have used the third-order accurate Fer expansion [19]; in the second step, simple operator splitting; and the numerical integration procedure

$$\int_{k\delta t}^{(k+1)\delta t} \mathrm{d}t'\ \mathcal{F}_{t'} \approx \mathcal{F}_{k\delta t}\delta t + \mathcal{O}(\delta t^2)\ , \tag{29}$$

in the third step. It is important to apply the operators in a time-ordered product series, which is indicated by the arrow above the product sign. The obtained method will be first-order accurate if it is stable and the numerical procedure for each operator (streaming and forcing) is at least second-order accurate. The total error arises since the matrices $A^{(i)}\partial_{x_i}$ and M_V are in general not commuting and because of the second-order accurate integration procedure. For a second-order accurate method we write

$$\vec{a}^*(t,\vec{x}) \approx \prod_{k=0}^{\overleftarrow{N_t-1}} e^{\mathcal{S}\delta t} \exp\left(\int_{k\delta t}^{(k+1)\delta t} \mathrm{d}t' \ \mathcal{F}_{t'}\right) \vec{a}_0^*(\vec{x}), \quad (30)$$
$$\vec{a}^*(t,\vec{x}) \equiv e^{-\frac{1}{2}\mathcal{F}_t\delta t}\vec{a}(t,\vec{x}) \ ,$$

where we have used the Strang-splitting [20]. To achieve the demanded accuracy we have to use a third-order accurate integration formula for the forcing operation, whereas second-order accuracy in the definition of a^* is sufficient, because it acts only twice during the evolution. If the potential has an explicit time-dependence one can use the midpoint rule,

$$\int_{k\delta t}^{(k+1)\delta t} \mathrm{d}t' \ \mathcal{F}_{t'} \approx \mathcal{F}_{(k+\frac{1}{2})\delta t}\delta t + \mathcal{O}(\delta t^3) \ . \quad (31)$$

For the Wigner-Poisson problem [21] where one needs to determine the self-consistent electro-static potential, $\Delta V = e\rho(t,\vec{x})$, at every time-step, we make use of the fact that the forcing operation does not change the density and hence the electro-static potential. Taking Eq. (15) and integrating by parts we can show

$$\int_{\mathbb{R}^d} \mathrm{d}\vec{v} \ \ (\partial_t W + \Theta[V]W) = \partial_t \rho = 0 \ . \quad (32)$$

Consequently, if the numerical procedure in this step conserves the density up to $\mathcal{O}(\delta t^3)$, it will be sufficient to recalculate the forcing operator after each streaming, which coincides with our time-step definition in Eq. (30). The questions that remain to be solved are how to compute approximations of the operators' actions $e^{\mathcal{S}\delta t}\vec{a}$ ("streaming") and $e^{\mathcal{F}_k\delta t}\vec{a}$ ("forcing") such that the resulting algorithm is stable, computationally efficient, and of the desired accuracy (first- or second-order).

B. Forcing

As it was mentioned in section II A, the matrix M_V is skew-hermitian, which means that it belongs to the Lie algebra of the group of unitary matrices. Depending on the basis choice we might also find the subgroups of special unitary or special orthogonal matrices if M_V is a traceless, skew-Hermitian, complex matrix or a real, skew-symmetric one. Hence, the action of the forcing operator is a *unitary rotation* of the coefficient vector, whose matrix form can in general be calculated before starting the simulation. For a skew-symmetric matrix one could use the method described in Ref. [22] or a Padé approximation [23]

$$e^{\mathcal{F}_{k\delta t}\delta t} \approx \left[\mathbf{1} + \frac{\delta t}{2}M_V(k\delta t,\vec{x})\right]^{-1}\left[\mathbf{1} - \frac{\delta t}{2}M_V(k\delta t,\vec{x})\right] \ .$$

For the case of the Wigner-Poisson problem one needs to compute the product of matrix times vector at every time-step, which for instance can be efficiently done with the "Expokit" software package [24] or using a precalculated explicit formula.

One might be tempted to use explicit schemes, such as Euler or Runge-Kutta, to approximate the forcing. However, these methods can become unstable for strongly changing potentials and poor temporal and spatial resolution, which we will show for two examples by evaluating the amplification factor g in von Neumann's stability analysis [25]. Consider a time-independent one-dimensional anharmonic potential and the Euler as well as the fourth-order Runge-Kutta method (RK4) as approximations of the forcing, whose amplification factors are given by

$$g_{\mathrm{Euler}} = |\mathbf{1} - \delta t M_V(x)|_2 \ , \quad (33)$$
$$g_{\mathrm{RK4}} = |\mathbf{1} + \sum_{j=1}^{4} \frac{[-\delta t M_V(x)]^j}{j!}|_2 \ , \quad (34)$$

where $|\dots|_2$ stands for the 2- or spectral-norm, such that Parseval's identity is applicable. The plots for both methods are shown in Fig. 1. One observes the big amplification factor at the domain boundary, caused by the strong potential variation in this area, cf. Fig. 2, which may eventually trigger a numerical instability.

C. Streaming

The streaming can in general be achieved by methods handling (non-)linear hyperbolic systems of conservation laws, often used in computational fluid dynamics, such as finite difference, volume, elements or lattice Boltzmann [26]. Using, for example, in $d = 1$ a flux vector splitting [27], we first diagonalize the matrix $A^{(1)} = TD_AT^{-1}$. Then we define the new coefficient vector $\vec{b}(t,\vec{x}) \equiv T^{-1}\vec{a}(t,\vec{x})$ and the modified forcing term $\tilde{M}_V \equiv T^{-1}M_VT$, such that the new system of partial differential equations can be written as

$$\partial_t\vec{b} + D_A\partial_x\vec{b} + \tilde{M}_V(t,\vec{x})\vec{b} = \vec{0} \ . \quad (35)$$

To simulate the action of the streaming operator, one can now employ the first-order accurate upwind or the second-order accurate Lax-Wendroff scheme [13], since $A^{(1)}$ only has real eigenvalues, i.e. D_A is a real diagonal

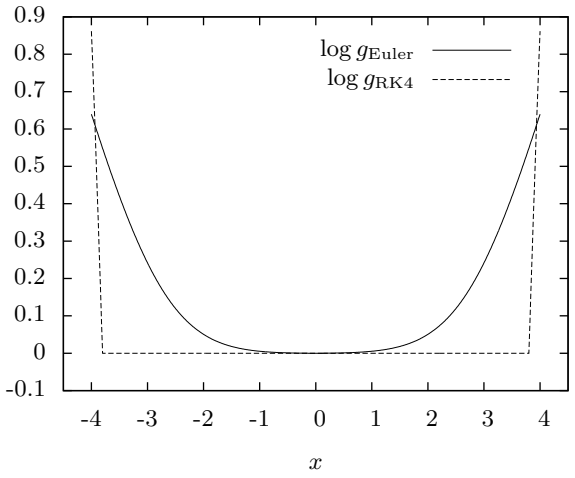

FIG. 1. Amplification factor for an anharmonic potential ($K = 0.5$) using Euler ($1/\delta x = 100$) and RK4 ($1/\delta x = 50$) methods with $N = 10$.

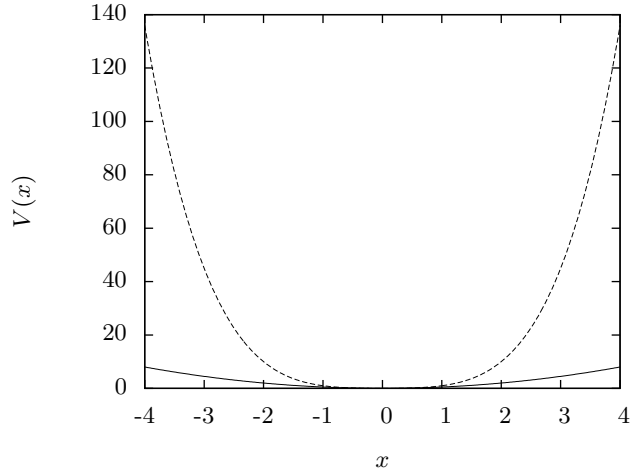

FIG. 2. Dimensionless anharmonic potential for $K = 0$ (solid) and $K = 0.5$ (dashed).

matrix. The drawbacks of the explicit methods are that the Courant-Friedrichs-Levy condition

$$\frac{|\lambda|_{max}\delta t}{\delta x} \leq 1 \ , \tag{36}$$

needs to be fulfilled for a stable simulation (*conditional stability*) and that they introduce a considerable amount of dissipation, especially if structures with large gradients are streamed [13]. If we are employing Hermite functions we could - in the spirit of the lattice Boltzmann method [28–30] - use an "exact" streaming operation, which will mitigate the dissipative effects. For this we perform a discrete Hermite transform in $\vec{v}$-space[31] from the coefficient vector to the Wigner function, stream, and transform back to the coefficient vector. However, a more detailed analysis and implementation will be the topic of a subsequent article.

D. Stability

The proposed method for evolving the Wigner function will be stable if the operations streaming and forcing are both stable. Since the action of the forcing can be described as a unitary rotation one should make sure that the numerical technique conserves this property and hence has an amplification factor of unity. In that respect, the skew-hermiticity of M_V, the matrix representation of $\Theta[V]$, is a crucial property for the stability of such algorithms, which we will demonstrate in appendix B for an asymmetric Hermite basis. This may require a very accurate result for the rotation matrix or the usage of Clifford algebras [32] to perform the rotation. However, the least computationally expensive operation is the direct matrix-vector multiplication $\mathcal{O}(N^2)$, whereas the use of the algebra will need slightly more operations (although the scaling is the same). For the streaming, one can use any stable method that handles linear advection equations, such as flux vector splitting [27], Godunov, finite volume or finite element [13]. The resulting time-evolution of the Wigner function will hence be stable.

IV. SIMULATION

For the validation of our numerical procedure we simulate the time-evolution of an (an-)harmonic oscillator. The advantages of these examples are that, on one hand, we can compare with the analytical Wigner function of a harmonic oscillator, which is calculated as described in Ref. [16]. On the other hand, we can observe the effects of quantum corrections to the classical dynamics for an anharmonic potential $U_{\mathrm{anh}}(\vec{q}) = \frac{1}{2}m\omega|\vec{q}|^2 + \frac{m^2\omega^3 K}{\hbar}|\vec{q}|^4$ [2]. In the case of the double well potential $U_{\mathrm{mh}}(\vec{q}) = cm\omega|\vec{q}|^2 + \frac{m^2\omega^3 K}{\hbar}|\vec{q}|^4$ we can observe the tunneling phenomenon in the Wigner formalism, since for certain parameter ranges $c < 0$ and $K > 0$ the system has states with eigenenergies below 0 which would not allow classical particles to travel from one potential minimum to the other. As we have described in the introduction to the Wigner formalism, see section II, we use a dimensionless form of the Schrödinger and Wigner equations. For our examples, we take $l \equiv \sqrt{\frac{\hbar}{m\omega}}$, $T \equiv \frac{1}{\omega}$ and $\bar{U} \equiv \hbar\omega$ as length, time, and potential scales, respectively, to find $\epsilon = 1$ and $B = 1$. The dimensionless time-dependent Schrödinger equation reads

$$\imath\partial_t\Psi = \left(\frac{|\hat{\vec{v}}|^2}{2} + c|\hat{\vec{x}}|^2 + K|\hat{\vec{x}}|^4\right)\Psi \ , \tag{37}$$

such that the eigenfunctions and -values of the dimensionless Hamilton operator at $K = 0$ and $c = 1/2$ are

given by

$$\Psi_n^{|n|}(\vec{x}) = \frac{e^{-|\vec{x}|^2/2}}{\sqrt{\pi^{d/2}2^{|n|}n!}} H_n^{|n|}(\vec{x}) \ , \tag{38}$$

$$\mathcal{E}_n = |n| + d/2 \ , \tag{39}$$

where $n = (n_1, \ldots, n_d)$ is a multi-index and

$$H_n^{|n|}(\vec{x}) = (-1)^{|n|} e^{|\vec{x}|^2} \left(D^k e^{-|\vec{x}|^2} \right) \ , \tag{40}$$

the d-dimensional Hermite polynomial, according to Ref. [33]. The dimensionless Wigner equation in differential form becomes

$$\partial_t W + \vec{v} \cdot \vec{\nabla}_x W - 2(c + 2K|\vec{x}|^2)\vec{x} \cdot \vec{\nabla}_v W + \Theta_c[K]W = 0 \ , \tag{41}$$

where

$$\Theta_c[K]W \equiv \frac{K}{4} \sum_{|\lambda|=3} \frac{D_x^\lambda |\vec{x}|^4}{\lambda!} D_v^\lambda W \tag{42}$$

is the quantum correction to the "classical" dynamics of the particle.

A. Basis of Hermite functions

In our simulation, we choose Hermite functions as orthonormal basis set in momentum-space, i.e.

$$\phi_k^{|k|}(\vec{v}) = \frac{e^{-|\vec{v}|^2/2}}{\sqrt{\pi^{d/2}2^{|k|}k!}} H_k^{|k|}(\vec{v}) \ , \tag{43}$$

where k is a multi-index of dimension d. Hence, Eq. (19) changes to

$$W(t, \vec{x}, \vec{v}) = \sum_{|k|=0}^{N} a_k^{|k|}(t, \vec{x}) \ \phi_k^{|k|}(\vec{v}) \ . \tag{44}$$

The number of basis functions that is needed to simulate the evolution of a given state will in general depend on how wide the spread of the corresponding Wigner function is in momentum space. However, by scaling the Hermite functions, cf. Ref. [34], one can significantly reduce N to simulate eigenstates with higher energy. In order to find the necessary number of basis functions for a chosen accuracy one needs to take a look at the variation of the resulting Wigner function with respect to changes in N. In order to find the initial coefficients, $\vec{a}(t_0, \vec{x})$, we use the property of the Hermite polynomials or Hermite functions, defined by Eq. (43), that they diagonalize the Fourier transform operator,

$$\int_{\mathbb{R}^d} \mathrm{d}\vec{v} \ e^{\imath \vec{y} \cdot \vec{v}/\epsilon} \phi_k^{|k|}(\vec{v}) = (\sqrt{2\pi})^d \imath^{|k|} \phi_k^{|k|}(\vec{y}) \ . \tag{45}$$

The proof is given in Ref. [16]. Using the Wigner transform, defined by Eq. (8), we can write

$$\begin{aligned} a_k^{|k|}(t_0, \vec{x}) &= \int_{\mathbb{R}^d} \mathrm{d}\vec{v} \ W(t_0, \vec{x}, \vec{v}) \phi_k^{|k|}(\vec{v}) \ , \\ &= \int_{\mathbb{R}^d} \mathrm{d}\vec{y} \ \Psi^* \left(t_0, \vec{x} + \frac{\epsilon \vec{y}}{2} \right) \Psi \left(t_0, \vec{x} - \frac{\epsilon \vec{y}}{2} \right) \phi_k^{|k|}(\vec{y}) \\ &\quad \times \frac{\epsilon^d \imath^{|k|}}{(2\pi)^{\frac{d}{2}}} \ . \end{aligned}$$

One can see that the obtained coefficients are real due to the symmetry properties of the Hermite functions $\phi_k^{|k|}(-\vec{y}) = (-1)^{|k|} \phi_k^{|k|}(\vec{y})$. In addition, we can simplify Eq. (23) by using the same property to obtain

$$(M_V)_{k,l} = \frac{B}{\epsilon} \imath^{|k|-|l|-1} \int_{\mathbb{R}^d} \mathrm{d}\vec{\eta} \ \delta V(t, \vec{x}, \vec{\eta}) \phi_k^{|k|}(\vec{\eta}) \phi_l^{|l|}(\vec{\eta}) \ . \tag{46}$$

Looking at this result, one can realize that M_V is a real, skew-symmetric matrix. The matrices $A^{(i)}$ are real, symmetric and *sparse* for this basis choice. They are sparse, because, regardless how the basis functions are ordered at most two entries per row or column are non-zero due to the recursion relation of the d-dimensional Hermite polynomials [33]. For further explanations on the conservation and convergence properties for this basis choice, we refer the reader to Ref. [34], where the authors treat the Vlasov equation, which can be considered as the classical limit, $\epsilon \to 0$, of the Wigner equation.

B. Harmonic oscillator

We run a simulation of an one-dimensional harmonic oscillator with the second order accurate method, using a Lax-Wendroff scheme for the streaming, a spatial resolution of $\delta x = 1/50$, and periodic boundaries at $x = \pm 3.5$. The resulting matrices for the reaction-advection system can be calculated using formula (A1) in appendix A. As initial state Ψ we choose a superposition between ground and first excited state $\frac{\Psi_0 + \Psi_1}{\sqrt{2}}$, since the Wigner function of a single eigenstate is time-independent. Thus, we can observe the evolution for a system whose probability density changes in time. In Fig. 3, we show a comparison between the analytical spatial probability density $\rho_\Psi(t, x) \equiv |\Psi(t, x)|^2$ and the probability density calculated from the Wigner function with

$$\rho_W(t, x) \equiv \int_{\mathbb{R}} \mathrm{d}v \ W(t, x, v) = \sum_{k=0}^{N} a_k(t, x) \int_{\mathbb{R}} \mathrm{d}v \ \phi_k(v) \ .$$

The comparison shows very good agreement. However, the actual results for the Wigner function are more insightful, since they contain additional information. They are shown in Figs. 4-8 together with the contour lines

at $W = 0$ and $W = \pm 0.025$. One observes a "rigid" rotation of the Wigner function in phase space, which is typical for the harmonic oscillator. This can be seen by using the method of characteristics for solving Eq. (41) at $K = 0$ and $c = 0.5$ which leads to solving the Hamilton equations

$$\dot{x} = v \ , \ \dot{v} = -x \ . \tag{47}$$

The period for one revolution is $T = 2\pi(\mathcal{E}_1 - \mathcal{E}_0) = 2\pi$, which is also confirmed by the simulation in terms of the temporal error margin. The contour line at $W = 0$ close to the boundaries shows patterns which are not present in the analytical solution. They are caused by the numerical error fluctuations, see Fig. 9, since the magnitude of the Wigner function in that region becomes comparable to the numerical error.

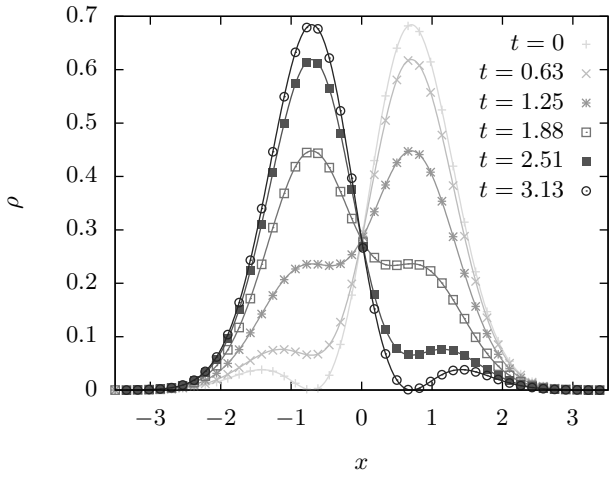

FIG. 3. Temporal evolution of the probability density for the harmonic potential ($c = 0.5$, $K = 0$), ρ_Ψ (solid lines) and ρ_W (points) for $\Psi = (\Psi_0 + \Psi_1)/\sqrt{2}$ using $N = 16$ Hermite basis functions.

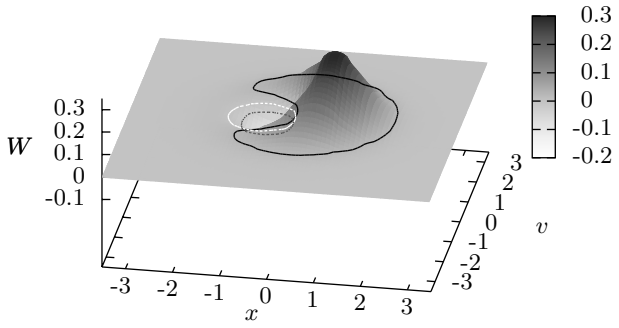

FIG. 4. Wigner function for the harmonic potential ($c = 0.5$, $K = 0$) at $t = 0$ for the superposition $\Psi = (\Psi_0 + \Psi_1)/\sqrt{2}$ using $N = 16$ Hermite basis functions; contour lines at $W = 0$ (white) and $W = \pm 0.025$ (black/gray).

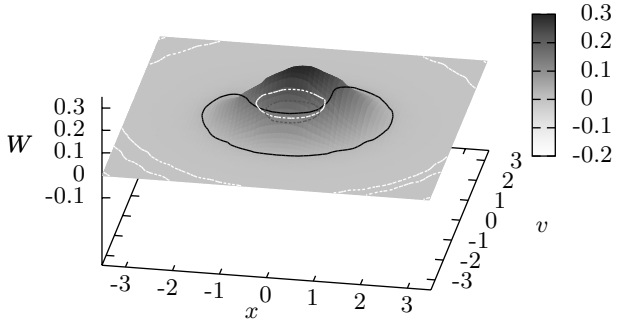

FIG. 5. Wigner function for the harmonic potential ($c = 0.5$, $K = 0$) at $t = 1.25$ for the superposition $\Psi = (\Psi_0 + \Psi_1)/\sqrt{2}$ using $N = 16$ Hermite basis functions; contour lines at $W = 0$ (white) and $W = \pm 0.025$ (black/gray).

C. Convergence

Based on the work in Ref. [16], one can calculate the exact Wigner transform $W_{\rm ex}$ of any wave function $\Psi(t, \vec{x})$ expanded in Hermite functions. We will use this formula to calculate the Wigner transform for an eigenstate $\Psi_n(t, x)$ of the harmonic oscillator and compare our results for different numbers of basis functions N and spatial resolutions $1/\delta x$. It is important to note that the exact Wigner function of an eigenstate for $K = 0$, $c = 0.5$ and $d = 1$ is given by Laguerre polynomials through

$$W_n(x, v) = \frac{(-1)^n}{\pi} L_n[2(x^2 + v^2)] e^{-x^2 - v^2} \ , \tag{48}$$

$$L_n(y) \equiv \frac{1}{n!} \left(\frac{\mathrm{d}}{\mathrm{d}x} - 1 \right)^n x^n \ , \tag{49}$$

which does not give a finite expansion into Hermite functions in v. The deviation of our results from the analytical solution after one period is shown in Fig. 9. We observe that the error is of the order of 10^{-4} and its magnitude is rather homogeneously distributed. In Fig. 10 we show the convergence of the second order accurate

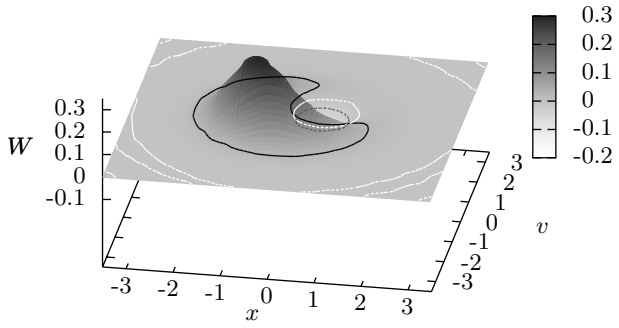

FIG. 6. Wigner function for the harmonic potential ($c = 0.5$, $K = 0$) at $t = 2.51$ for the superposition $\Psi = (\Psi_0 + \Psi_1)/\sqrt{2}$ using $N = 16$ Hermite basis functions; contour lines at $W = 0$ (white) and $W = \pm 0.025$ (black/gray).

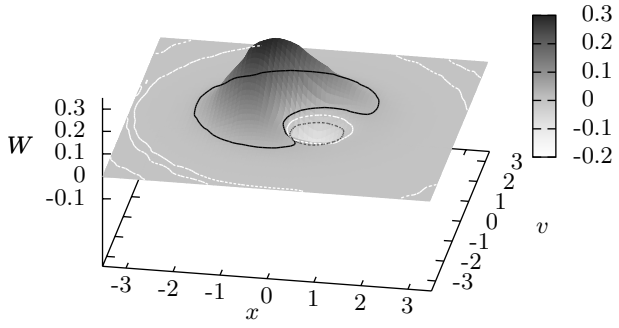

FIG. 7. Wigner function for the harmonic potential ($c = 0.5$, $K = 0$) at $t = 3.76$ for the superposition $\Psi = (\Psi_0 + \Psi_1)/\sqrt{2}$ using $N = 16$ Hermite basis functions; contour lines at $W = 0$ (white) and $W = \pm 0.025$ (black/gray).

method by looking at the error

$$\Delta \equiv \sqrt{\frac{1}{N_x N_v} \sum_{i,j} |\Delta W(x_i, v_j, t)|^2} \,, \qquad (50)$$

$$\Delta W(x_i, v_j, t) \equiv W(x_i, v_j, t) - W_{\mathrm{ex}}(x_i, v_j, t) \,, \qquad (51)$$

for periodic boundary conditions in real-space and a domain size $x \in [-5, 5]$. The error is evaluated by choosing the same momentum- and space-grid. The domain size is chosen such that boundary effects do not significantly influence the error in the convergence analysis,

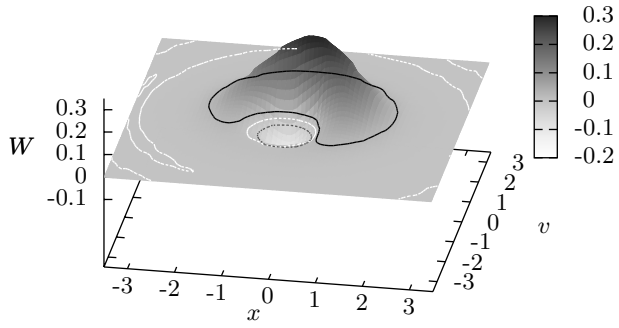

FIG. 8. Wigner function for the harmonic potential ($c = 0.5$, $K = 0$) at $t = 5.01$ for the superposition $\Psi = (\Psi_0 + \Psi_1)/\sqrt{2}$ using $N = 16$ Hermite basis functions; contour lines at $W = 0$ (white) and $W = \pm 0.025$ (black/gray).

since $W(t, \pm 5, v) \sim \mathcal{O}(10^{-10})$. Looking at Fig. 10, we observe that the second order convergence can only be verified for sufficiently many basis functions (here: $N = 32$). This behavior is caused by a total error that is composed by the discretization of time and real-space as well as the approximation of the Wigner function with a finite number of basis functions in momentum-space. Therefore, we expect Δ to saturate for a fixed resolution and an increasing number of basis functions, or in the opposite scenario, which can be deduced from Fig. 10 for $N = 16$.

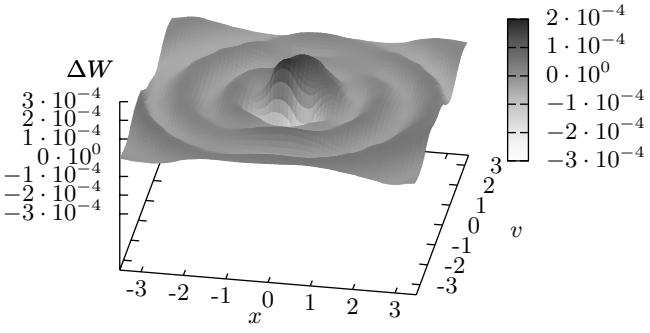

FIG. 9. Error of the Wigner function for the harmonic potential ($c = 0.5$, $K = 0.5$) at $t = 6.28$ for the superposition $\Psi = (\Psi_0 + \Psi_1)/\sqrt{2}$ with $N = 16$, $\delta x = 1/50$.

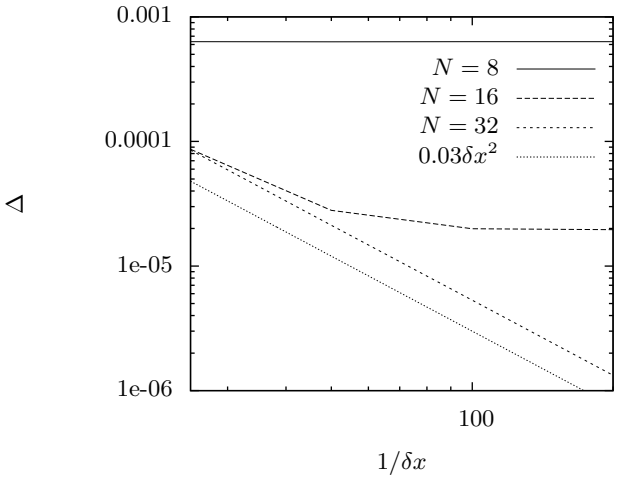

FIG. 10. Convergence analysis of the harmonic Wigner function after $t = 2\pi$ with respect to δx and N_b.

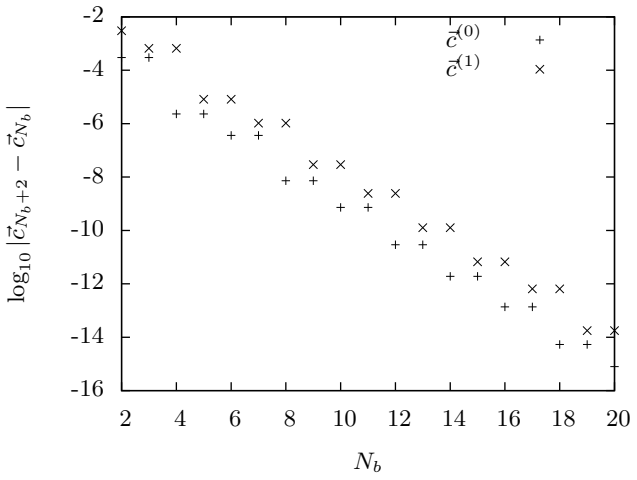

FIG. 11. Convergence of eigenstate coefficient vector for ground and first excited states of the anharmonic potential ($c = 0.5$, $K = 0.001$) up to *double precision*.

D. Anharmonic oscillator

For an anharmonic potential $c = 0.5$ and $K > 0$ we approximate the eigenstates $\Psi_n^{(an)}$ by a superposition of N_b harmonic eigenstates, i.e.

$$\Psi_n^{(an)}(t,x) \approx e^{-\imath t \mathcal{E}_n^{(an)}} \sum_{k=0}^{N_b} c_k^{(n)} \Psi_k(x) \ . \tag{52}$$

Then we determine the coefficient vector $\vec{c}^{(n)}$ by diagonalizing the matrix representation of the anharmonic Hamilton operator. This works very well for moderate anharmonicities, but becomes very costly for $K > 10^{-3}$, as can be seen in Figs. 11 and 12. In addition, one also observes that, as expected, the ground state converges faster than the first excited state.

The simulation is run with the second order accurate method for periodic boundary conditions at $x = \pm 3.5$ with a spatial resolution of $1/\delta x = 50$. The result for the spatial probability evolution is shown in Fig. 13, where we observe a good agreement with the wave function dynamics. In Figs. 14-18 we show the Wigner function evolution together with the contour lines at $W = 0$ and $W = \pm 0.025$. They depict a "rotation" with a smaller period $T_{an} = 2\pi/(\mathcal{E}_1^{(an)} - \mathcal{E}_0^{(an)}) < 2\pi$. In this case it is not a rigid rotation, since the Wigner function gets compressed in position- and broadened in momentum-space due to the larger potential and the particle number conservation. The contour line at $W = 0$ close to the boundaries shows again the numerical error fluctuations, since in this region the magnitude of the Wigner function becomes comparable to the error, which is $\mathcal{O}(10^{-4})$. It was estimated by comparing the initial and final Wigner function of one revolution.

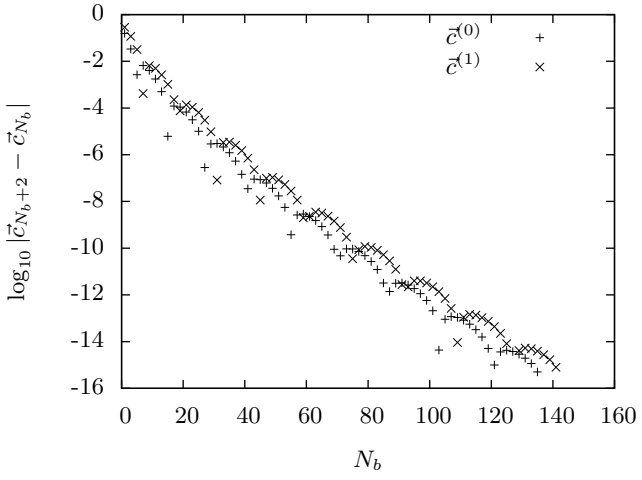

FIG. 12. Convergence of eigenstate coefficient vector for ground and first excited states of the anharmonic potential ($c = 0.5$, $K = 0.5$) up to *double precision*.

E. Double well potential

To study tunneling effects, we simulate the time-evolution of the Wigner function for "bounded" states of a one-dimensional double well potential $V(x) = cx^2 + Kx^4$, cf. Fig. 19, with the second order accurate method, periodic boundary conditions at $x = \pm 4$ and spatial resolution $1/\delta x = 50$. We call a state bounded if its eigenenergy is smaller than zero and hence below the potential barrier around $x = 0$. Taking again the Hermite basis to approximate the ground and first excited state as in Eq. (52), we show in Fig. 20 the evolution of the prob-

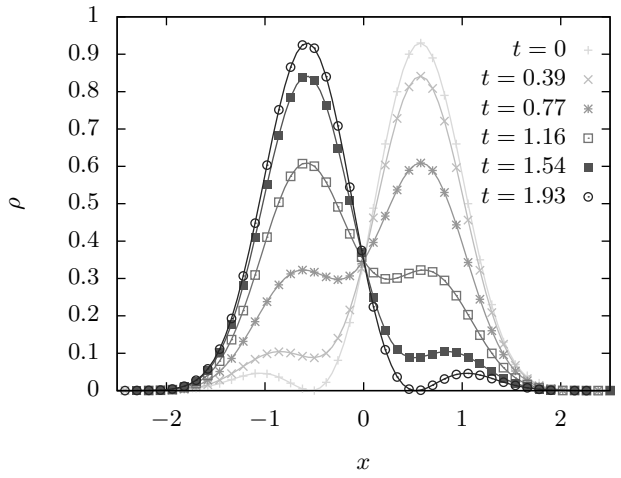

FIG. 13. Temporal evolution of the probability density for the anharmonic potential ($c = 0.5$, $K = 0.5$), ρ_Ψ (solid lines) and ρ_W (points) for $\Psi = (\Psi_0^{(an)} + \Psi_1^{(an)})/\sqrt{2}$ using $N_b = 150$, and $N = 16$ Hermite basis functions.

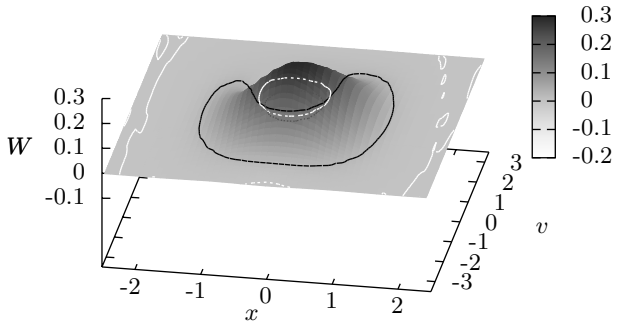

FIG. 15. Wigner function for the anharmonic potential ($c = 0.5$, $K = 0.5$) at $t = 0.77$ for the superposition $\Psi = (\Psi_0^{(an)} + \Psi_1^{(an)})/\sqrt{2}$ using $N_b = 150$, and $N = 16$ Hermite basis functions; contour lines at $W = 0$ (white) and $W = \pm 0.025$ (black/gray).

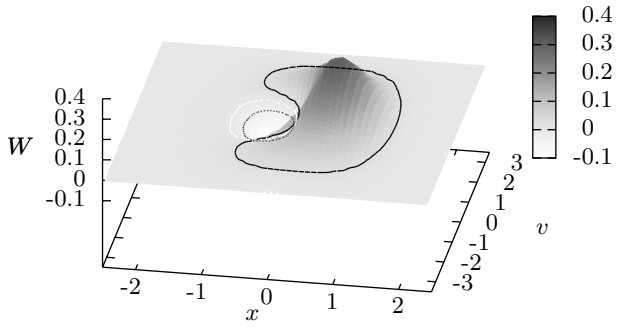

FIG. 14. Wigner function for the anharmonic potential ($c = 0.5$, $K = 0.5$) at $t = 0$ for the superposition $\Psi = (\Psi_0^{(an)} + \Psi_1^{(an)})/\sqrt{2}$ using $N_b = 150$, and $N = 16$ Hermite basis functions; contour lines at $W = 0$ (white) and $W = \pm 0.025$ (black/gray).

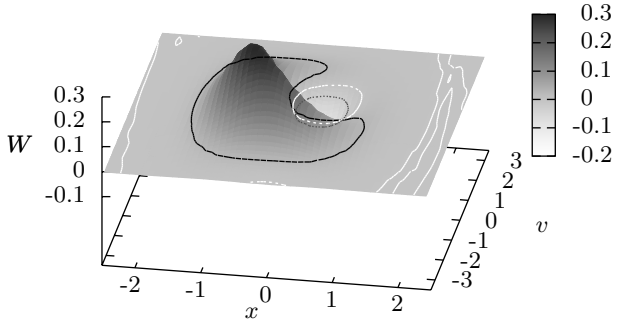

FIG. 16. Wigner function for the anharmonic potential ($c = 0.5$, $K = 0.5$) at $t = 1.54$ for the superposition $\Psi = (\Psi_0^{(an)} + \Psi_1^{(an)})/\sqrt{2}$ using $N_b = 150$, and $N = 16$ Hermite basis functions; contour lines at $W = 0$ (white) and $W = \pm 0.025$ (black/gray).

ability density in comparison to the evolution according to Schrödinger's equation. The agreement is very good. In Figs. 21-25 one can see the evolution of the Wigner function for the tunneling of the state through the potential barrier together with contour lines at $W = 0$ and $W = \pm 0.025$. The error during the revolution is at most $\mathcal{O}(10^{-4})$, as can be seen in Fig. 26. In addition, one observes by looking at the contour line for $W = -0.025$ the appearance of ripples and valleys in the front and the back of the positive quasi-probability density during the tunneling process of the particle through the potential barrier, which indicate the non-classical behavior in the corresponding coordinate space. The contour line at $W = 0$ close to the boundaries shows again the numerical error fluctuations in regions where the magnitude of the Wigner function becomes comparable to the numerical error. The period of the revolution $T_{mh} = 2\pi/(\mathcal{E}_1^{(mh)} - \mathcal{E}_0^{(mh)}) \gg 2\pi$ is much larger than the

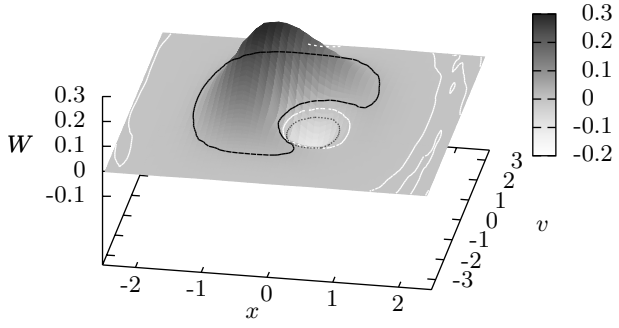

FIG. 17. Wigner function for the anharmonic potential ($c = 0.5$, $K = 0.5$) at $t = 2.23$ for the superposition $\Psi = (\Psi_0^{(an)} + \Psi_1^{(an)})/\sqrt{2}$ using $N_b = 150$, and $N = 16$ Hermite basis functions; contour lines at $W = 0$ (white) and $W = \pm 0.025$ (black/gray).

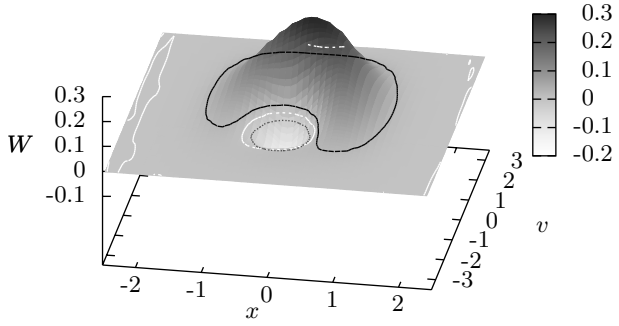

FIG. 18. Wigner function for the anharmonic potential ($c = 0.5$, $K = 0.5$) at $t = 3.09$ for the superposition $\Psi = (\Psi_0^{(an)} + \Psi_1^{(an)})/\sqrt{2}$ using $N_b = 150$, and $N = 16$ Hermite basis functions; contour lines at $W = 0$ (white) and $W = \pm 0.025$ (black/gray).

one for a harmonic oscillator. In addition to the probability density and the Wigner function, we have also analyzed the spread of the Wigner function in phase space by measuring the expectation values

$$(\Delta x^2)(\Delta v^2) \equiv \langle(\hat{x} - \langle\hat{x}\rangle)^2\rangle\langle(\hat{v} - \langle v\rangle)^2\rangle \quad (53)$$

$$= \left(\langle x^2\rangle_W - \langle x\rangle_W^2\right)\left(\langle v^2\rangle_W - \langle v\rangle_W^2\right) , \quad (54)$$

$$\mathrm{Cov}(x,v) \equiv \left(\frac{1}{2}\langle\hat{x}\hat{v} + \hat{v}\hat{x}\rangle - \langle\hat{x}\rangle\langle\hat{v}\rangle\right)/(\Delta x \Delta v) \quad (55)$$

$$= \frac{\langle xv\rangle_W - \langle x\rangle_W\langle v\rangle_W}{\sqrt{\langle x^2\rangle_W - \langle x\rangle_W^2}\sqrt{\langle v^2\rangle_W - \langle v\rangle_W^2}} , \quad (56)$$

where $\langle f(x,v)\rangle_W \equiv \int \mathrm{d}x\mathrm{d}v \; f(x,v)W$. The first quantity measures the well-known standard deviation of a quantum state in coordinate and momentum space that fulfills Heisenberg's uncertainty principle $\Delta x \Delta v \geq \frac{\epsilon}{2}$. In Fig. 27 we show the coordinate and momentum uncertainty in the form of rectangles, i.e. the width, height and aread correspond to Δx, Δv and $\Delta x \Delta v$, respectively. In that way, one can see that the standard deviation in position measurements mainly contributes to the uncertainty and its temporal change. The second quantity $\mathrm{Cov}(x,v)$ is the covariance between the coordinate and momentum variable in the corresponding Wigner function normalized with the standard deviations, such that $|\mathrm{Cov}(x,v)| \leq 1$. The evolution of these expectaton values is shown in Fig. 28. One observes a periodic behavior with $T = T_{mh}/2$ and finds the maximum uncertainty $\Delta x \Delta v$ exactly when the peak of the spatial probability density tunnels through the potential barrier in the middle of the double well potential. In contrast $\mathrm{Cov}(x,v)$ behaves similar to the first temporal derivative of the uncertainty.

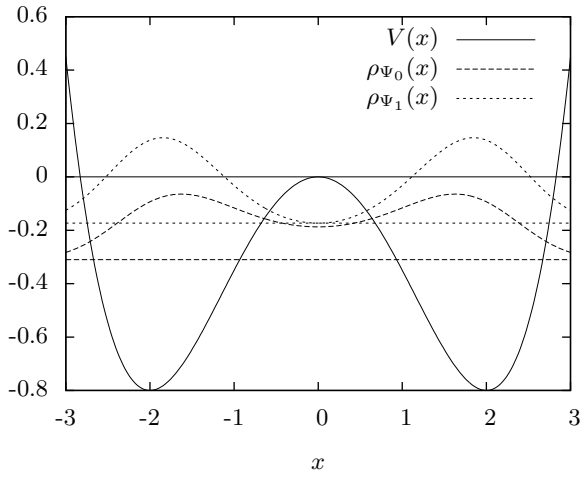

FIG. 19. Double well potential ($c = -0.4$, $K = 0.05$) and probability density of ground and first excited states displaced from 0 by $\mathcal{E}_0^{(mh)} = -0.310$ (dashed horizontal line) and $\mathcal{E}_1^{(mh)} = -0.173$ (dotted horizontal line) for $N_b = 86$ Hermite basis functions.

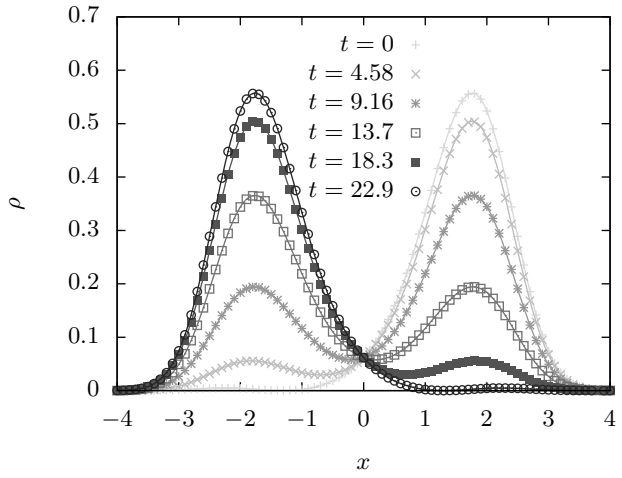

FIG. 20. Temporal evolution of the probability density for the double well potential ($c = -0.4$, $K = 0.05$), ρ_Ψ (solid lines) and ρ_W (points) for the superposition $\Psi = (\Psi_0^{(mh)} + \Psi_1^{(mh)})/\sqrt{2}$ using $N_b = 86$, and $N = 32$ Hermite basis functions.

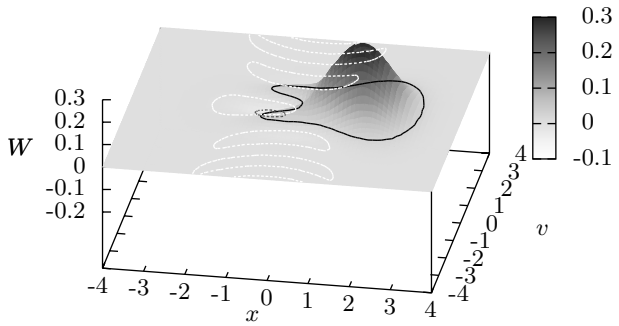

FIG. 21. Wigner function for the double well potential ($c = -0.4$, $K = 0.05$) at $t = 0$ for the superposition $\Psi = (\Psi_0^{(mh)} + \Psi_1^{(mh)})/\sqrt{2}$ using $N_b = 86$, and $N = 32$ Hermite basis functions; contour lines at $W = 0$ (white) and $W = \pm 0.025$ (black/gray).

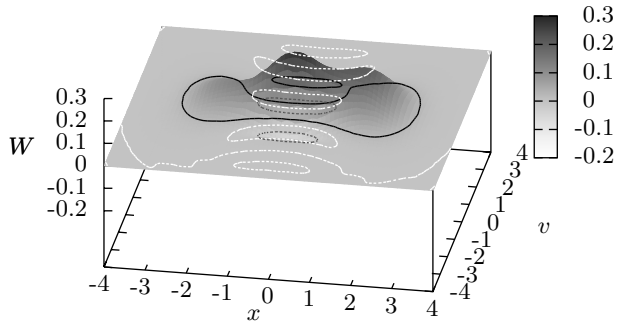

FIG. 22. Wigner function for the double well potential ($c = -0.4$, $K = 0.05$) at $t = 9.16$ for the superposition $\Psi = (\Psi_0^{(mh)} + \Psi_1^{(mh)})/\sqrt{2}$ using $N_b = 86$, and $N = 32$ Hermite basis functions; contour lines at $W = 0$ (white) and $W = \pm 0.025$ (black/gray).

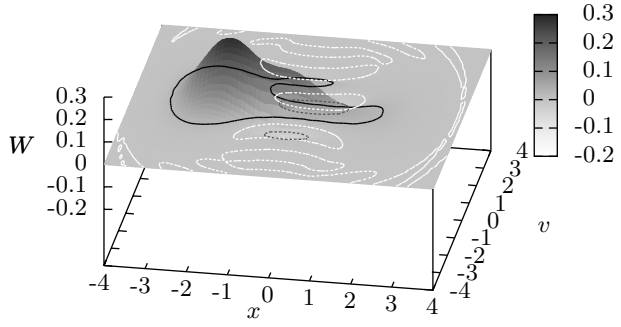

FIG. 23. Wigner function for the double well potential ($c = -0.4$, $K = 0.05$) at $t = 18.3$ for the superposition $\Psi = (\Psi_0^{(mh)} + \Psi_1^{(mh)})/\sqrt{2}$ using $N_b = 86$, and $N = 32$ Hermite basis functions; contour lines at $W = 0$ (white) and $W = \pm 0.025$ (black/gray).

V. CONCLUSIONS

We have developed a semi-spectral simulation method for the time-evolution of the Wigner quasi-probability distribution that uses a spectral-decomposition of the distribution into arbitrary basis functions of $L^2(\mathbb{R}^d)$ in momentum-space, which transforms the original partial differential equation into an infinite-dimensional set of advection-reaction equations.

For the numerical treatment, we introduce a cut-off in the expansion, which makes the system finite-dimensional, and split the operators for the reaction and advection part so as to apply them sequentially to the distribution function. We demonstrated that, due to the skew-hermitian symmetry of the matrix representation of the pseudo-differential operator (Lie algebra), the action of the forcing or reaction operator (Lie group) is

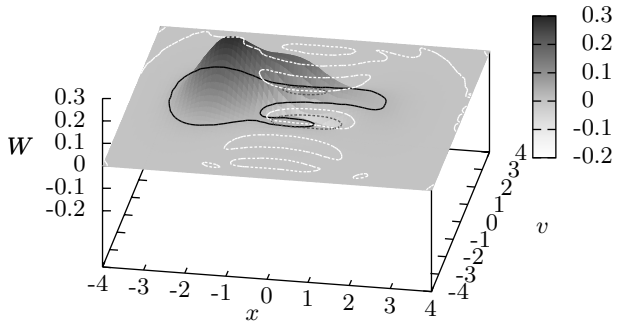

FIG. 24. Wigner function for the double well potential ($c = -0.4$, $K = 0.05$) at $t = 27.5$ for the superposition $\Psi = (\Psi_0^{(mh)} + \Psi_1^{(mh)})/\sqrt{2}$ using $N_b = 86$, and $N = 32$ Hermite basis functions; contour lines at $W = 0$ (white) and $W = \pm 0.025$ (black/gray).

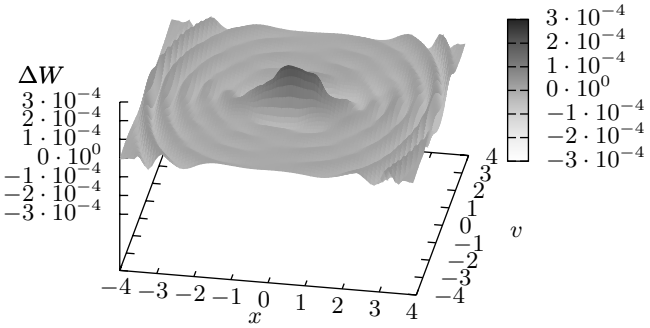

FIG. 26. Error of the simulated Wigner function for the double well potential ($c = -0.4$, $K = 0.05$) at $t = 45.9$ for the superposition $\Psi = (\Psi_0^{(mh)} + \Psi_1^{(mh)})/\sqrt{2}$ using $N_b = 86$, and $N = 32$ Hermite basis functions.

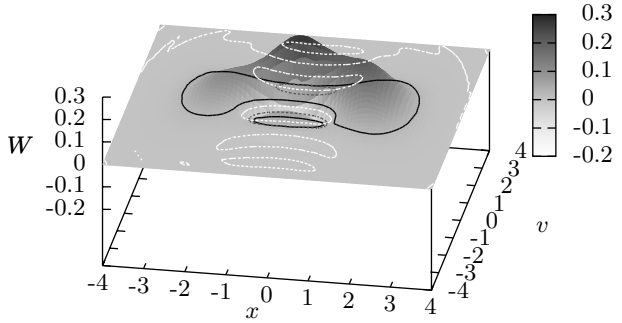

FIG. 25. Wigner function for the double well potential ($c = -0.4$, $K = 0.05$) at $t = 36.7$ for the superposition $\Psi = (\Psi_0^{(mh)} + \Psi_1^{(mh)})/\sqrt{2}$ using $N_b = 86$, and $N = 32$ Hermite basis functions; contour lines at $W = 0$ (white) and $W = \pm 0.025$ (black/gray).

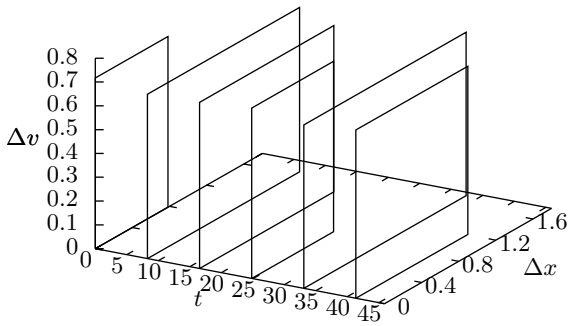

FIG. 27. Temporal evolution of the spread in the form of rectangles (width $\equiv \Delta x$, height $\equiv \Delta v$, area $\equiv \Delta x \Delta v$) of the simulated Wigner function for the double well potential ($c = -0.4$, $K = 0.05$) for the superposition $\Psi = (\Psi_0^{(mh)} + \Psi_1^{(mh)})/\sqrt{2}$ using $N_b = 86$, and $N = 32$ Hermite basis functions.

a unitary rotation, which stabilizes the simulation even for strongly varying potentials compared to other explicit methods, such as Euler or RK4. The advection or streaming part can be handled by many numerical approaches from computational fluid dynamics. Here, we have chosen a flux-vector splitting for the validation of our method by simulating a single, non-relativistic, spinless particle subject to a one-dimensional (an-)harmonic or double well potential with Hermite basis functions. Having the exact Wigner function of the harmonic oscillator, we verified the second-order convergence of the method and also demonstrated its applicability to nonclassical dynamics in the case of strong anharmonicities and tunneling phenomena.

The disadvantage of an arbitary basis choice is the higher computational cost of $\mathcal{O}(N^2)$ compared to $\mathcal{O}(N \log N)$ for a Fourier basis, since the pseudo-differential operator is diagonal for this basis choice, as shown in Refs. [7, 8] . However, if one only considers

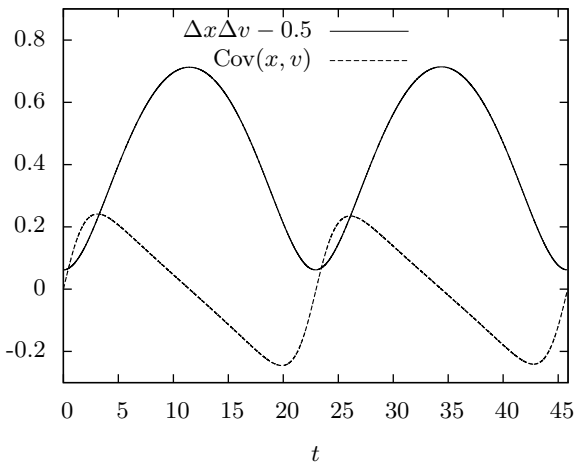

FIG. 28. Temporal evolution of the uncertainty (solid) and covariance (dashed) of the simulated Wigner function for the double well potential ($c = -0.4$, $K = 0.05$) for the superposition $\Psi = (\Psi_0^{(mh)} + \Psi_1^{(mh)})/\sqrt{2}$ using $N_b = 86$, and $N = 32$ Hermite basis functions.

momentum-derivatives up to order $N_\lambda \ll N$ and an explicit scheme such as fourth order Runge-Kutta is used, the computational cost also scales like $\mathcal{O}(N)$ [34]. In addition, the artificial periodization of the Wigner distribution in momentum-space, caused by the plane wave approximation, lives in a different function space than the original Wigner function, thus giving rise to unphysical self-interactions at the domain boundaries [15]. These basis functions are also not well suited to the simulation of structures that are strongly localized in momentum-space, such as particles in periodic potentials, since this would require a very large number of such functions.

The CPU time for the time evolution of one revolution for the harmonic Wigner function, using the second-order accurate method with $N = 32$ Hermite basis functions and a spatial resolution $1/\delta x = 100$, i.e. 700 grid points and 4558 time-steps, is approximately 7.92 s using a single core of a 3 GHz Intel(R) Core(TM)2 Quad CPU Q9650 processor.

As future work, we plan to study phase transitions in *open quantum systems*, the effects of scattering ("*quantum Boltzmann equation*"), for example in the case of electrons and phonons in semiconductor devices, the effects of boundary conditions, cf. Ref. [5], and stochastic perturbations. Furthermore, we plan to analyse the influence of decoherence on the topology of the Wigner function in two dimensions, cf. Ref. [35].

ACKNOWLEDGMENTS

Financial support from the European Research Council (ERC) Advanced Grant 319968-FlowCCS is kindly acknowledged.

[1] C. K. Zachos, D. B. Fairlie, and T. L. Curtright, editors. *Quantum Mechanics in Phase Space: An Overview with Selected Papers*, volume 34 of *World Scientific Series in 20th Century Physics*. World Scientific, 2005.

[2] E. Wigner. On the quantum correction for thermodynamic equilibrium. *Physical Review*, 40:749-759, 06 1932.

[3] D. Guilini, E. Joos, C. Kiefer, J. Kupsch, I.-O. Stamatescu, and H. D. Zeh. *Decoherence and the Appearance of a Classical World in Quantum Theory*. Springer, 1996.

[4] B. Duplantier, J.-M. Raimond, and V. Rivasseau, editors. *Quantum Decoherence PoincÃ¡re Seminar 2005*, volume 48 of *Progress in Mathematical Physics*. Birkhäuser, 2005.

[5] W. R. Frensley. Boundary conditions for open quantum systems driven far from equilibrium. *Review of Modern Physics*, 62(745), July 1990.

[6] K.-Y. Kim and B. Lee. On the high order numerical calculation schemes for the Wigner transport equation. *Solid-State Electronics*, 43:2243-2245, 1999.

[7] C. Ringhofer. A spectral method for the numerical simulation of quantum tunneling phenomena. *SIAM Journal of Numerical Analysis*, 27(1):32-50, 02 1990.

[8] A. Arnold and C. Ringhofer. Operator splitting methods applied to spectral discretizations of quantum transport equations. *SIAM Journal of Numerical Analysis*, 32(6):1876-1894, December 1995.

[9] B. Niclot, P. Degond, and F. Poupaud. Deterministic Particle Simulations of the Boltzmann Transport Equation of Semiconductors . *Journal of Computational Physics*, 78:313-350, 1988.

[10] C.-Y. Wong. Explicit solution of the time evolution of the Wigner function. *Journal of Optics B: Quantum and Semiclassical Optics*, 5:420-428, 2003.

[11] J. M. Sellier and I. Dimov. A Wigner Monte Carlo approach to density functional theory. *Journal of Computational Physics*, 270:265-277, 2014.

[12] J. M. Sellier and I. Dimov. On the simulation of indistinguishable fermions in the many-body Wigner formalism. *Journal of Computational Physics*, 280:287-294, 2015.

[13] R. Löhner. *Applied Computational Fluid Dynamics Techniques: An Introduction based on Finite Elements Methods*. John Wiley & Sons Ltd., 2nd edition, 2008.

[14] B.S. Kandemir. Wigner functions of an electron moving in a one-dimensional periodic potential. *Physics Letters A*, 245:209-219, 1998.

[15] S. Shao, T. Lu, and W. Cai. Adaptive Conservative Cell Average Spectral Element Methods for Transient Wigner Equation in Quantum Transport. *Communications Computational Physics*, 9(3):711-739, March 2011.

[16] H.J. Groenewold. On the principles of elementary quantum mechanics. *Physica*, 12(7):405-460, 1946.

[17] C. A. Ringhofer, D. K. Ferry, and N. Kluksdahl. Absorbing Boundary Conditions for the Simulation of Quantum

Transport Phenomena. *Transport Theory and Statistical Physics*, 18(3):331-346, 1989.

[18] L. Hörmander. *The analysis of linear partial differential operators I*, volume 256 of *Grundlagen Mathematische Wissenschaften*. Springer, 1983.

[19] A. Iserles, H. Munthe-Kaas, S. Norsett, and A. Zanna. Lie-group methods. *Acta Numerica*, 8:1-199, March 1999.

[20] G. Strang. On the construction and comparison of difference schemes. *SIAM Journal of Numerical Analysis*, 5:506-517, 1968.

[21] P. A. Markowich, C. A. Ringhofer, and C. Schmeiser. *Semiconductor Equations*. Springer, 1990.

[22] J. Gallier and D. Xu. Computing exponentials of skew-symmetric matrices and logarithms of orthogonal matrices. *International Journal of Robotics and Automation*, 17(4), 2002.

[23] C. Moler and C. Van Loan. Nineteen dubious ways to compute the exponential of a matrix, twenty-five years later . *SIAM Review*, 45(1):3-49, March 2003.

[24] R. B. Sidje. EXPOKIT: A software Package for Computing Matrix Exponentials. *AcM-Transactions on Mathematical Software*, 245(1):130-156, 1998.

[25] E. Isaacson and H. B. Keller. *Analysis of numerical methods*. Dover Publications, 1994.

[26] R. Benzi, S. Succi, and M. Vergassola. The lattice Boltzmann equation: theory and applications. *Physics Reports*, 222(3):145-197, 1992.

[27] J. L. Steger and R. F. Warming. Flux Vector Splitting of the Inviscid Gasdynamic Equations with Application to Finite-Difference Methods. *Journal of Computational Physics*, 40:263-293, 1981.

[28] H. Grad. On the kinetic theory of rarefied gases. *Communications on Pure and Applied Mathematics*, 2(4):331-407, December 1949.

[29] S. Succi. *The Lattice Boltzmann Equation for Fluid Dynamics and Beyond*. Numerical Mathematics and Scientific Computation. Oxford University Press, 2009.

[30] M. Mendoza, B. M. Boghosian, H. J. Herrmann, and S. Succi. Fast Lattice Boltzmann Solver for Relativistic Hydrodynamics. *Phys. Rev. Lett.*, 105:014502, 2010.

[31] G. Leibon, D. N. Rockmore, W. Park, R. Taintor, and G. S. Chirikjian. A fast Hermite transform. *Theoretical Computer Science*, 409:211-228, 2008.

[32] J. Snygg. *Clifford Algebra A Computational Tool for Physicists*. Oxford Univ Pr, January 1997.

[33] H. Grad. Note on N-Dimensional Hermite Polynomials. *Communications on Pure and Applied Mathematics*, 2(4):325-330, December 1949.

[34] J. W. Schumer and J. P. Holloway. Vlasov Simulations Using Velocity-Scaled Hermite Representations. *Journal of Computational Physics*, 144:626-661, 1998.

[35] O. Steuernagel, D. Kakofengitis, and G. Ritter. Wigner flow reveals topological order in quantum phase space. *Physical Review Letters*, 110(030401), 2013.

[36] J. P. Holloway. Spectral velocity discretizations for the Vlasov-Maxwell equations. *Transport Theory and Statistical Physics*, 25(1):1-32, 1996.

[37] G. Joyce, G. Knorr, and H. K. Meier. Numerical Integration Methods of the Vlasov Equation. *Journal of Computational Physics*, 8:53-63, 1971.

[38] Cheng and Knorr. The integration of the Vlasov Equation in Configuration Space. *Journal of Computational Physics*, 22:330-351, 1976.

Appendix A: Matrix-representation of pseudo-differential operator

For a one-dimensional, analytical potential and the Hermite function basis the matrix-representation of the pseudo-differential operator simplifies from Eq. (46) to

$$M_V = \sum_{n=0}^{\infty} \left(\frac{\epsilon}{2}\right)^{2n} M_n \partial_x^{2n+1} V(t,x) \ , \tag{A1}$$

$$(M_n)_{k,l} \equiv \imath^{k-l-1} \int_{\mathbb{R}} \mathrm{d}\eta \ \frac{\eta^{2n+1}}{(2n+1)!} \phi_k(\eta)\phi_l(\eta) \ .$$

Looking at this result one observes how the contributions from odd higher order derivatives scale with the effective Planck constant and the change in sign. The examples for $N = 5$ shows the filling of higher order matrices with more and more entries. In the case of $N = 5$, the matrix M_V is already filled for $n = 2$, i.e. considering the fifth derivative of the potential. As soon as M_V is completely filled an explicit method, such as Euler or Runge-Kutta will have a computational complexity of $\mathcal{O}(N^2)$, although the prefactor will be smaller than for the method which uses the corresponding rotation matrix.

$$M_0 = \begin{pmatrix} 0 & -\frac{1}{\sqrt{2}} & 0 & 0 & 0 & 0 \\ \frac{1}{\sqrt{2}} & 0 & -1 & 0 & 0 & 0 \\ 0 & 1 & 0 & -\sqrt{\frac{3}{2}} & 0 & 0 \\ 0 & 0 & \sqrt{\frac{3}{2}} & 0 & -\sqrt{2} & 0 \\ 0 & 0 & 0 & \sqrt{2} & 0 & -\sqrt{\frac{5}{2}} \\ 0 & 0 & 0 & 0 & \sqrt{\frac{5}{2}} & 0 \end{pmatrix}$$

$$M_1 = \begin{pmatrix} 0 & -\frac{1}{4\sqrt{2}} & 0 & \frac{1}{4\sqrt{3}} & 0 & 0 \\ \frac{1}{4\sqrt{2}} & 0 & -\frac{1}{2} & 0 & \frac{1}{2\sqrt{3}} & 0 \\ 0 & \frac{1}{2} & 0 & -\frac{3\sqrt{\frac{3}{2}}}{4} & 0 & \frac{\sqrt{\frac{5}{6}}}{2} \\ -\frac{1}{4\sqrt{3}} & 0 & \frac{3\sqrt{\frac{3}{2}}}{4} & 0 & -\sqrt{2} & 0 \\ 0 & -\frac{1}{2\sqrt{3}} & 0 & \sqrt{2} & 0 & -\frac{5\sqrt{\frac{5}{2}}}{4} \\ 0 & 0 & -\frac{\sqrt{\frac{5}{6}}}{2} & 0 & \frac{5\sqrt{\frac{5}{2}}}{4} & 0 \end{pmatrix}$$

$$M_2 = \begin{pmatrix} 0 & -\frac{1}{32\sqrt{2}} & 0 & \frac{1}{16\sqrt{3}} & 0 & -\frac{1}{16\sqrt{15}} \\ \frac{1}{32\sqrt{2}} & 0 & -\frac{3}{32} & 0 & \frac{\sqrt{3}}{16} & 0 \\ 0 & \frac{3}{32} & 0 & -\frac{19}{32\sqrt{6}} & 0 & \frac{\sqrt{\frac{5}{6}}}{4} \\ -\frac{1}{16\sqrt{3}} & 0 & \frac{19}{32\sqrt{6}} & 0 & -\frac{11}{16\sqrt{2}} & 0 \\ 0 & -\frac{\sqrt{3}}{16} & 0 & \frac{11}{16\sqrt{2}} & 0 & -\frac{17\sqrt{\frac{5}{2}}}{32} \\ \frac{1}{16\sqrt{15}} & 0 & -\frac{\sqrt{\frac{5}{6}}}{4} & 0 & \frac{17\sqrt{\frac{5}{2}}}{32} & 0 \end{pmatrix}$$

Appendix B: Example for unstable "basis" choice

Assuming we are dealing with a harmonic potential, then the quantum corrections vanish and the Wigner and

Vlasov equation are identical. Using an asymmetric Hermite basis, as described in [36], i.e.

$$W(t,x,v) = \frac{e^{-v^2}}{\pi^{1/4}} \sum_{k=0}^{N} a_k(t,x) \frac{H_k(v)}{\sqrt{2^n n!}} \ , \qquad \text{(B1)}$$

the matrix representation of $\Theta[V]$ will be lower triangular, which can be seen using formula (15) and integration by parts. For $N = 4$ we find

$$M_V(x) = -x \begin{pmatrix} 0 & 0 & 0 & 0 & 0 \\ \sqrt{2} & 0 & 0 & 0 & 0 \\ 0 & 2 & 0 & 0 & 0 \\ 0 & 0 & \sqrt{6} & 0 & 0 \\ 0 & 0 & 0 & 2\sqrt{2} & 0 \end{pmatrix}$$

which is not skew-hermitian or -symmetric anymore. Examining the resulting exact forcing action, we find

$$e^{-M_V(x)\delta t} = \begin{pmatrix} 1 & 0 & 0 & 0 & 0 \\ \sqrt{2}x\delta\mathrm{t} & 1 & 0 & 0 & 0 \\ \sqrt{2}x^2\delta\mathrm{t}^2 & 2x\delta\mathrm{t} & 1 & 0 & 0 \\ \frac{2x^3\delta\mathrm{t}^3}{\sqrt{3}} & \sqrt{6}x^2\delta\mathrm{t}^2 & \sqrt{6}x\delta\mathrm{t} & 1 & 0 \\ \sqrt{\frac{2}{3}}x^4\delta\mathrm{t}^4 & \frac{4x^3\delta\mathrm{t}^3}{\sqrt{3}} & 2\sqrt{3}x^2\delta\mathrm{t}^2 & 2\sqrt{2}x\delta\mathrm{t} & 1 \end{pmatrix}$$

from which we conclude for the amplification factor

$$g_{\mathrm{AS}} = \left| e^{-M_V(x)\delta t} \right|_2 > 1 \text{ if } \delta t > 0 \ , \ x \neq 0 \ .$$

This means that the method will become unstable at a certain time in the evolution, as described in Ref. [34]. There are ways to tackle this problem by introducing a collision operator, see Ref. [37], or a filtering technique, further explained in Ref. [38].